

# In Situ Observation of Room-Temperature Magnesium Metal Deposition on a NASICON/IL Hybrid Solid Electrolyte

Zhixuan Wei,\* Dheeraj Kumar Singh, Katharina Helmbrecht, Joachim Sann, Yuriy Yusim, Joy A. Kieser, Clarissa Glaser, Marcus Rohnke, Axel Groß,\* and Jürgen Janek\*

Secondary batteries using multivalent cations as ionic charge carriers have attracted increasing attention in recent years due to the high theoretical energy density provided by multi-electron redox reactions. However, the high charge density of these cations inevitably leads to sluggish kinetics of ion migration at room temperature, which poses a challenge for the development of solid-state batteries using multivalent ions. Here, a magnesium ion conducting hybrid solid electrolyte (HSE) is prepared, consisting of a new NASICON-structured material,  $\text{Mg}_{0.5}\text{Sn}_2(\text{PO}_4)_3$ , and a small amount of magnesium ionic liquid. The HSE shows superior room-temperature ionic conductivity of  $1.11 \times 10^{-4} \text{ S cm}^{-1}$  and an activation energy of 0.36 eV. Due to the good compatibility of the HSE with the magnesium metal anode, symmetric  $\text{Mg}|\text{HSE}|\text{Mg}$  cells show stable magnesium plating and stripping behavior at room temperature. Using in situ electrochemical scanning electron microscopy measurements, the room temperature growth-induced fracture of the HSE is observed, giving unequivocal evidence for magnesium deposition. These results may serve as a starting point for understanding the magnesium deposition mechanism on solid electrolytes in solid-state batteries.

reactions.<sup>[1–5]</sup> This advantage makes them an attractive supplement to the existing lithium-ion battery (LIB) technology, especially in environments where the energy storage system is limited by space constraints and, hence needs to be compact. Not at least, the mentioned elements are abundant and may lead to cost-effective and resource-uncritical cell concepts. Among various MV-ion-based energy storage concepts, the development of rechargeable Mg batteries (RMBs) has witnessed great progress since the first working battery prototype was reported in 2000.<sup>[6]</sup> Apart from the merits of the low cost of Mg as well as the low redox potential of  $\text{Mg}^{2+}/\text{Mg}$  (−2.36 V vs SHE), it has been generally believed – although debated – that Mg deposition is less prone to dendrite formation, compared with the lithium counterpart.<sup>[7–9]</sup> This makes the utilization of the Mg metal anode with the high volumetric capacity more


## 1. Introduction

Rechargeable batteries with multivalent ions (MV =  $\text{Mg}^{2+}$ ,  $\text{Ca}^{2+}$ ,  $\text{Zn}^{2+}$ ,  $\text{Al}^{3+}$ , etc.) as charge carriers have attracted significant research interest in the past decade owing to the high theoretical volumetric energy density provided by multi-electron redox

appealing, and long cycle life may be expected. Unfortunately, unlike in the case of the solid electrolyte interface (SEI) in LIBs, the sluggish solid-state diffusion of densely charged  $\text{Mg}^{2+}$  ions makes it a major challenge to seek appropriate electrolytes that can form a  $\text{Mg}^{2+}$ -conducting interlayer on the surface of the Mg metal anode.<sup>[10]</sup> In the case of monovalent cations,

Z. Wei, D. K. Singh, J. Sann, Y. Yusim, J. A. Kieser, C. Glaser, M. Rohnke, J. Janek  
Institute of Physical Chemistry  
Justus Liebig University Giessen  
Heinrich-Buff-Ring 17, 35392 Giessen, Germany  
E-mail: zhixuan.wei@phys.chemie.uni-giessen.de;  
juergen.janek@phys.chemie.uni-giessen.de

Z. Wei, D. K. Singh, J. Sann, Y. Yusim, J. A. Kieser, C. Glaser, M. Rohnke, J. Janek  
Center for Materials Research (LaMa)  
Justus Liebig University Giessen  
Heinrich-Buff-Ring 16, 35392 Giessen, Germany  
K. Helmbrecht, A. Groß  
Institute of Theoretical Chemistry  
Ulm University  
Oberberghof 7, 89081 Ulm, Germany  
E-mail: axel.gross@uni-ulm.de  
A. Groß  
Helmholtz Institute Ulm (HIU) for Electrochemical Energy Storage  
Helmholtzstraße 11, 89081 Ulm, Germany

 The ORCID identification number(s) for the author(s) of this article can be found under <https://doi.org/10.1002/aenm.202302525>

© 2023 The Authors. Advanced Energy Materials published by Wiley-VCH GmbH. This is an open access article under the terms of the Creative Commons Attribution-NonCommercial-NoDerivs License, which permits use and distribution in any medium, provided the original work is properly cited, the use is non-commercial and no modifications or adaptations are made.

DOI: 10.1002/aenm.202302525

solid-state batteries (SSBs) attract strong interest since the absence of flammable organic solvents may result in improved safety, by mitigating thermal runaway issues.<sup>[11,12]</sup> However, due to the mentioned issue of low  $\text{Mg}^{2+}$  ion mobility, it is challenging to achieve a sufficiently high  $\text{Mg}^{2+}$  conductivity at, or close to ambient temperature.

Therefore, designing solid electrolytes with high ionic conductivity is critical for the development of Mg-based SSBs. The knowledge gained in exploring superionic Li-ion conductors cannot be directly transferred to  $\text{Mg}^{2+}$ -ion conductors. As the magnesium analogs suffer from high  $\text{Mg}^{2+}$  migration barriers due to their strong electrostatic interaction with adjacent ions in the lattice,<sup>[1]</sup> one needs to find different design criteria to conquer the penalty of slow  $\text{Mg}^{2+}$  diffusion in solids. In early studies, efforts have been spent toward improving the  $\text{Mg}^{2+}$  conductivity in oxides, which possess high oxidation stability as well as chemical stability, along with low electronic conductivity.<sup>[13]</sup>  $\text{Mg}_{0.5}\text{Zr}_2(\text{PO}_4)_3$ , with  $\beta\text{-Fe}_2(\text{SO}_4)_3$  structure, was the first reported Mg-ion solid electrolyte.<sup>[14]</sup> The  $\text{ZrO}_6$  octahedra and  $\text{PO}_4$  tetrahedra are connected with each other via corner-sharing, giving rise to a 3-dimensional open framework for ion migration. However, an ionic conductivity of  $\sigma(\text{Mg}^{2+}) \approx 10^{-3} \text{ S cm}^{-1}$  is only achieved at 800 °C, with limited conductivity improvement upon aliovalent atom doping to increase defect concentration.<sup>[15,16]</sup> Computational studies suggest that NASICON-type structures can lead to lower activation energy and higher ionic conductivity compared to oxides with  $\beta\text{-Fe}_2(\text{SO}_4)_3$ -type structure, due to their increased structural symmetry.<sup>[17]</sup> For instance, NASICON-type  $(\text{Mg}_{0.1}\text{Hf}_{0.9})_{4/3,8}\text{Nb}(\text{PO}_4)_3$  exhibits an ionic conductivity of  $\sigma(\text{Mg}^{2+}) = 2.1 \times 10^{-6} \text{ S cm}^{-1}$  at 300 °C, which is 20 times higher than in case of the  $\beta\text{-Fe}_2(\text{SO}_4)_3$ -type  $\text{Mg}_{0.7}(\text{Zr}_{0.85}\text{Nb}_{0.15})_4(\text{PO}_4)_6$  solid electrolyte at the same temperature.<sup>[18]</sup> This indicates that NASICON-type materials with more stuffed  $\text{Mg}^{2+}$  atoms can possibly lead to higher Mg-ion conductivity.

Apart from the slow bulk Mg-ion conduction, the sluggish intergranular ion transport kinetics are another limiting factor in the development of Mg-based solid electrolytes. Studies in lithium SSBs indicate that liquid-phase additives can overcome the inherent solid-solid contact limitations both at the electrode interface and inside the bulk phases.<sup>[19,20]</sup> In this perspective, the unique physical properties of ionic liquids (ILs), e.g., their low flammability, low vapor pressure, and high ionic conductivity, make them attractive additives to modify the interfaces of solid electrolytes.<sup>[21]</sup> The obtained electrolytes, often called “pseudo-solid-state” electrolytes, combine an ion-conducting or non-conducting solid framework skeleton with room temperature ILs, also referred to as hybrid solid electrolytes or ionogels, respectively.<sup>[22]</sup> On top of increasing the ionic conductivity, the ILs can greatly improve the interfacial properties at both grain boundaries and the solid electrolyte/electrode interfaces.<sup>[23,24]</sup> In certain cases, the ILs also appear to suppress the chemical degradation of the solid electrolyte upon contact with the metal anode (see  $\text{Li}_{1.5}\text{Al}_{0.5}\text{Ge}_{1.5}(\text{PO}_4)_3$  as an example<sup>[25]</sup>).

In the present work, a new rhombohedral NASICON-structured phosphate,  $\text{Mg}_{0.5}\text{Sn}_2(\text{PO}_4)_3$ , was synthesized, where the main group metal Sn is selected to avoid kinetically favored reduction in contact with the metal anode that can be triggered

easily by transition metal elements.<sup>[26,27]</sup> Then, we designed a hybrid solid electrolyte (HSE) using  $\text{Mg}_{0.5}\text{Sn}_2(\text{PO}_4)_3$  as an Mg-ion conducting framework with 20 wt.% of IL (1 M magnesium bis[(trifluoromethyl)sulfonyl]imide ( $\text{Mg}(\text{TFSI})_2$ ) in 1-ethyl-3-methylimidazolium bis[(trifluoromethyl)sulfonyl]imide ( $(\text{EMIM})[\text{TFSI}])$ ). The obtained HSE shows an enhanced ionic conductivity of  $1.11 \times 10^{-4} \text{ S cm}^{-1}$  at room temperature with low activation energy,  $E_A = 0.36 \text{ eV}$ , which is  $10^5$  orders higher compared to pure “dry”  $\text{Mg}_{0.5}\text{Sn}_2(\text{PO}_4)_3$  ( $\sigma(\text{Mg}^{2+}) = 4.8 \times 10^{-9} \text{ S cm}^{-1}$ ). We attribute this to the improved inter-particle ion transport mediated by the IL. The obtained HSE facilitates Mg plating–stripping with high reversibility even at room temperature and long-term cycle stability, with a stable deposition overpotential of 600 mV. We also designed an electrochemical microcell to directly observe the Mg metal growth, which is composed of an Mg metal anode, the HSE as separator, and a tungsten needle (point radius of 0.35  $\mu\text{m}$ ) as cathode. To the best of our knowledge, Mg deposition is for the first time observed in situ in a solid-state cell by electrochemical scanning electron microscopy (SEM). Interestingly, different from the irregular lateral metal growth that is observed in lithium cells,<sup>[28]</sup> the deposition of Mg shows planar, smooth behavior across the interface with an overpotential of  $-1.9 \text{ V}$  at  $-5 \text{ nA}$ . We believe that the present results contribute significantly toward understanding the plating/deposition behavior at the Mg metal anode and propose design principles of room-temperature Mg SSBs.

## 2. Results and Discussion

### 2.1. Characterization of $\text{Mg}_{0.5}\text{Sn}_2(\text{PO}_4)_3$ Skeleton Material

$\text{Mg}_{0.5}\text{Sn}_2(\text{PO}_4)_3$  was synthesized by a modified sol-gel method. The detailed synthesis procedure can be found in the experimental section. The crystal structure of  $\text{Mg}_{0.5}\text{Sn}_2(\text{PO}_4)_3$  was studied by powder X-ray diffraction (XRD) with corresponding Rietveld refinement. As shown in Figure 1a, the reflection peaks can be well indexed based on a rhombohedral NASICON-type structure (space group  $R\bar{3}c$ ), with cell parameters of  $a = b = 8.54521 \text{ \AA}$ ,  $c = 21.64514 \text{ \AA}$ . The atomic parameters are listed in Table S1 (Supporting Information). Figure 1b exhibits the schematic refined crystal structure of  $\text{Mg}_{0.5}\text{Sn}_2(\text{PO}_4)_3$  in different directions, where the Mg atoms are half positioned at the  $6b$  (0, 0, 0) Wyck-off site. Nevertheless, several impurity peaks from a secondary phase were found at 19.2° and 22.2°. The hypothesis is that, due to the light molar mass as well as relatively low atomic fraction of Mg in the structure, the impurity might have originated from the inhomogeneous distribution of the Mg raw materials in the precursor. Therefore, we prepared materials with Mg excess and deficient stoichiometry, respectively, by the same method, to see whether the pure phase can be obtained. As shown in Figure S1a (Supporting Information), with an excess amount of the Mg source, the secondary phase does exhibit an increased peak intensity. This agrees well with the Rietveld refinement results (Figure S2 and Tables S1–S3, Supporting Information). As indicated by the structural occupancy of the Mg atom from the refinement result, even with more Mg content in the precursor, the Wyck-off position of  $6b$  cannot take up more Mg atoms. However, even with Mg deficiency in the precursor, the impurity phase could not

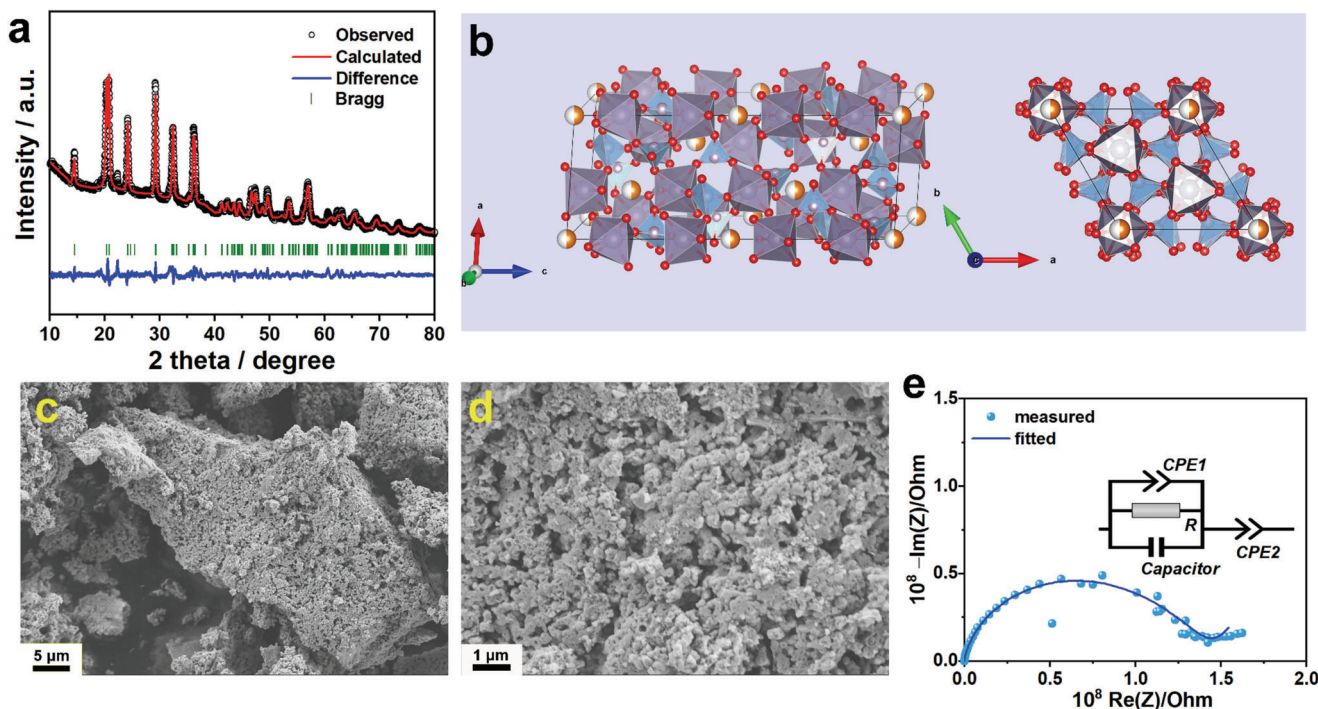


**Figure 1.** a) Rietveld refinement of the XRD pattern of  $\text{Mg}_{0.5}\text{Sn}_2(\text{PO}_4)_3$ ; b) crystal structure of  $\text{Mg}_{0.5}\text{Sn}_2(\text{PO}_4)_3$  in different directions, with orange spheres, blue tetrahedral, and purple octahedral exhibiting Mg,  $\text{PO}_4$  tetrahedra and  $\text{SnO}_6$  octahedra, respectively; c,d) SEM images of  $\text{Mg}_{0.5}\text{Sn}_2(\text{PO}_4)_3$  powder with different scales; e) Nyquist plot of  $\text{Mg}_{0.5}\text{Sn}_2(\text{PO}_4)_3$  in a symmetric cell configuration with stainless steel as ion blocking electrodes. The inset shows the equivalent circuit used to fit the plot.

be eliminated. After in-depth search and indexing, we initially assumed that the secondary phase is most likely  $\text{MgSn}(\text{OH})_6$ . Nevertheless, it seems questionable whether a hydroxide can exist at a sintering temperature of 800 °C. To this end, we increased the temperature to 1100 °C. As shown in Figure S1b (Supporting Information), the intensities of this secondary phase diffractions continue to grow, with the additional formation of a decomposition product,  $\text{SnO}_2$ . Therefore, it is more possible that the secondary phase is isostructural to  $\text{MgSn}(\text{OH})_6$ . However, further investigation still needs to be carried out to improve the purity of the  $\text{Mg}_{0.5}\text{Sn}_2(\text{PO}_4)_3$  material.

The morphology of as-prepared  $\text{Mg}_{0.5}\text{Sn}_2(\text{PO}_4)_3$  is shown in Figure 1c,d. Thanks to the citric acid-assisted liquid phase reaction, the product exhibits a hierarchical structure composed of nano-sized particles agglomerating into porous secondary particles, which is beneficial for the ionic liquid to penetrate and homogeneously distribute. The room-temperature ionic conductivity of the inorganic  $\text{Mg}_{0.5}\text{Sn}_2(\text{PO}_4)_3$  skeleton was first evaluated by electrochemical impedance spectroscopy (EIS), using stainless steel as ion-blocking electrodes. As shown in Figure 1e, the Nyquist plot exhibits one semicircle in the high-frequency range, representing the total resistance including both bulk and grain boundary resistance. Accordingly, the ionic conductivity is calculated to be  $\sigma(\text{Mg}^{2+}) = 4.8 \times 10^{-9} \text{ S cm}^{-1}$ , which is low, yet  $10^4$  times higher compared to  $\text{Mg}_{0.5}\text{Zr}_2(\text{PO}_4)_3$  with  $\beta\text{-Fe}_2(\text{SO}_4)_3$  structure (room temperature ionic conductivity of  $\sigma(\text{Mg}^{2+}) = 2.8 \times 10^{-13} \text{ S cm}^{-1}$ , as extrapolated from the Arrhenius plot from conductivities reported).<sup>[14]</sup>

## 2.2. Density-Functional Theory (DFT) Calculation of $\text{Mg}_{0.5}\text{Sn}_2(\text{PO}_4)_3$

To gain more insight into the ion migration behavior in the bulk structure of  $\text{Mg}_{0.5}\text{Sn}_2(\text{PO}_4)_3$ , DFT calculations were carried out. The crystal structure of  $\text{Mg}_{0.5}\text{Sn}_2(\text{PO}_4)_3$  is shown in a different way to better illustrate the ion hopping pathways, as shown in Figure 2a. The rhombohedral phase consists of 6 formula units in each unit cell and thus is comprised of 105 atoms. The relaxed lattice demonstrates cell parameters of  $a = b = 8.80 \text{ \AA}$  and  $c = 21.42 \text{ \AA}$ , which corroborates well with the experimental study. Per unit cell, the structure contains three Mg atoms which can be distributed equally among six different sites. The Mg sites are equivalent to the Na1 sites in a typical NASICON phase (the 6b Wyck-off site), which sit in an elongated octahedron with the equivalent Na2 sites left empty and only occupied during the cation diffusion through the cell. As there are three equal cations to be distributed among six different yet energetically equal sites, there are 20 distinct occupation patterns for the Mg cations. By comparing them energetically, the ordering in the cell was determined. The calculations show that the structures, where alternating sites are occupied which results in a maximum distance between the cations, are the most stable. They are closely followed in stability by those systems in which two neighboring sites are occupied, and the most unstable variations are present where the Mg cations sit right next to each other. However, the energies of the above structures vary by <10 meV per atom, which suggests that the preference for the cations to be spread equally inside the unit



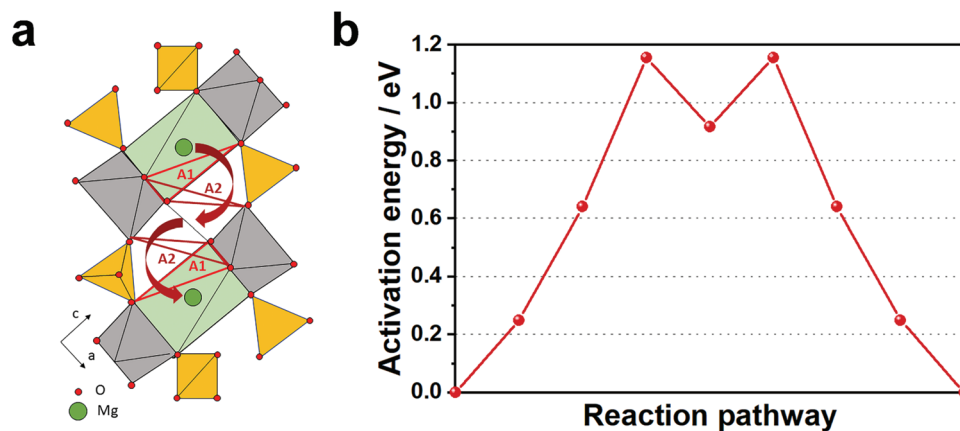


**Figure 2.** a) Representation of the diffusion pathway of the Mg ion through the NASICON-type structure. Mg moves through the first octahedra plane A1, then A2 into the unoccupied metastable “Na2” equivalent site, and then again through A2 and A1 into the neighboring Mg site. The bottleneck of the diffusion is determined to be A2 because of its slightly smaller size. The yellow tetrahedra and grey octahedra correspond to  $\text{PO}_4$  and the  $\text{SnO}_6$  units, respectively; b) exemplary NEB pathway of the diffusion event for one Mg moving through the two bottlenecks and the metastable intermediate.

cell without clustering is relatively small. It is worth noting that our preliminary results of an isostructural phase filled with Ca atoms show that the cations prefer to occupy the same site per unit cell multiple times, creating layers. Subsequently, the configuration of three layers being fully occupied followed by three completely empty appears to be most stable.

In a typical NASICON material, the Na cations diffuse through the Na1-Na2-Na1 pathway. In the Mg case, the only difference is that the “Na2” equivalent position is much less stable compared to “Na1” position, making it a metastable intermediate state. Therefore, a full diffusion process takes place between two neighboring “Na1” positions. To better describe the diffusion behavior, the properties of the triangular bottleneck are considered. Specifically, the bottleneck areas consist of three oxygen atoms in the  $\text{PO}_4$  tetrahedron and  $\text{SnO}_6$  octahedron, which are part of the diffusion pathway where the cation has to pass through the smallest opening of the structure.<sup>[29,30]</sup> As shown in Figure 2a, there are two bottlenecks in the pathway from “Na1” to “Na2”. The “Na2” octahedron is slightly smaller in this system, so it is the defining bottleneck with an area of  $4.35 \text{ \AA}^2$  and is marked as A2 in the figure. To estimate the barrier for diffusion without determining the whole minimum energy path between two Mg sites, we calculated the cell energy for the cation sitting exactly in this bottleneck area and compared it to the initial point of the diffusion pathway according to  $E_{\text{diff}} = E_{\text{bottleneck}} - E_{\text{ini}}$ . To get an accurate idea of the influence of the site occupation environment around the diffusion event, the barrier is determined for a unit cell with 1, 2, and 3 cations present.

The bottleneck calculations show that the barrier lies at 0.62, 0.48, and 0.14 eV for one to three charge carriers, respectively. This represents lower limits for the diffusion barriers. An exemplary nudged elastic band (NEB) calculation for the same diffusion shows a barrier of 1.16 eV for one charge carrier present (Figure 2b) and 0.71 eV for two charge carriers. The results indicate that the diffusion barrier is about twice as high as the pure system energy difference between the initial point and bottleneck position. Thus, we expect the diffusion barriers for three charge carriers in the unit cell to be of the order of 0.3 eV.

### 2.3. Ionic Conductivity of the Room-Temperature Hybrid Solid Electrolyte

By virtue of the relatively high ionic conductivity and favorable porous structure of the as-prepared  $\text{Mg}_{0.5}\text{Sn}_2(\text{PO}_4)_3$  skeleton, a hybrid solid electrolyte (HSE) was successfully prepared by blending  $\text{Mg}_{0.5}\text{Sn}_2(\text{PO}_4)_3$  with IL of 1 M magnesium bis[(trifluoromethyl)sulfonyl]imide ( $\text{Mg}(\text{TFSI})_2$ ) in 1-ethyl-3-methylimidazolium bis[(trifluoromethyl)sulfonyl]imide ([EMIM][TFSI]). As shown in Figure S3 (Supporting Information), Nyquist plots of samples with different weight ratios were recorded first. Remarkably, the room temperature ionic conductivity shows a sharp increase due to the infiltration of ionic liquid, most likely at the grain boundaries. By adding 10 wt.% of IL, the ionic conductivity increases to  $\sigma(\text{Mg}^{2+}) = 1.01 \times 10^{-5} \text{ S cm}^{-1}$ . At a ratio of 20 wt.% of IL, the conductivity value of this ratio reaches  $10^{-4} \text{ S cm}^{-1}$ . Since further adding IL does not provide a large increase in conductivity, the 20 wt.% fraction was used for further studies, and hereafter denoted as MgSP-HSE. As shown in the schematic illustration in Figure 3a, after the uptake of IL with a weight fraction of 20 wt.%, the MgSP-HSE still has the characteristics of a solid and remains a white powder. Besides, the cross-section photographic illustration of the dense pellet suggests good mechanical stability of HSE, derived from the MgSP ceramic framework. Figure 3b exhibits the Arrhenius plot of MgSP-HSE derived from the Nyquist plots collected at different temperatures (Figure S4, Supporting Information). Based on the Arrhenius equation, the activation energy is calculated to be 0.36 eV with a room temperature ionic conductivity of  $\sigma(\text{Mg}^{2+}) = 1.11 \times 10^{-4} \text{ S cm}^{-1}$ . In contrast, as shown in Figure S5 (Supporting Information), when blending the IL with the same weight percentage of non-ion-conducting  $\text{Al}_2\text{O}_3$ , the composite exhibits an ionic conductivity of  $\sigma(\text{Mg}^{2+}) = 4.45 \times 10^{-6} \text{ S cm}^{-1}$  at room temperature, which is two orders of magnitude lower than MgSP-HSE, indicating that the  $\text{Mg}^{2+}$  ion conduction in the HSE is mainly contributed by the NASICON framework.

As exemplified for Li/Na-ion conductors, an ionic conductivity of a solid electrolyte reaching  $10^{-4} \text{ S cm}^{-1}$  is enough for the function as separator material of a solid-state battery, while catholytes

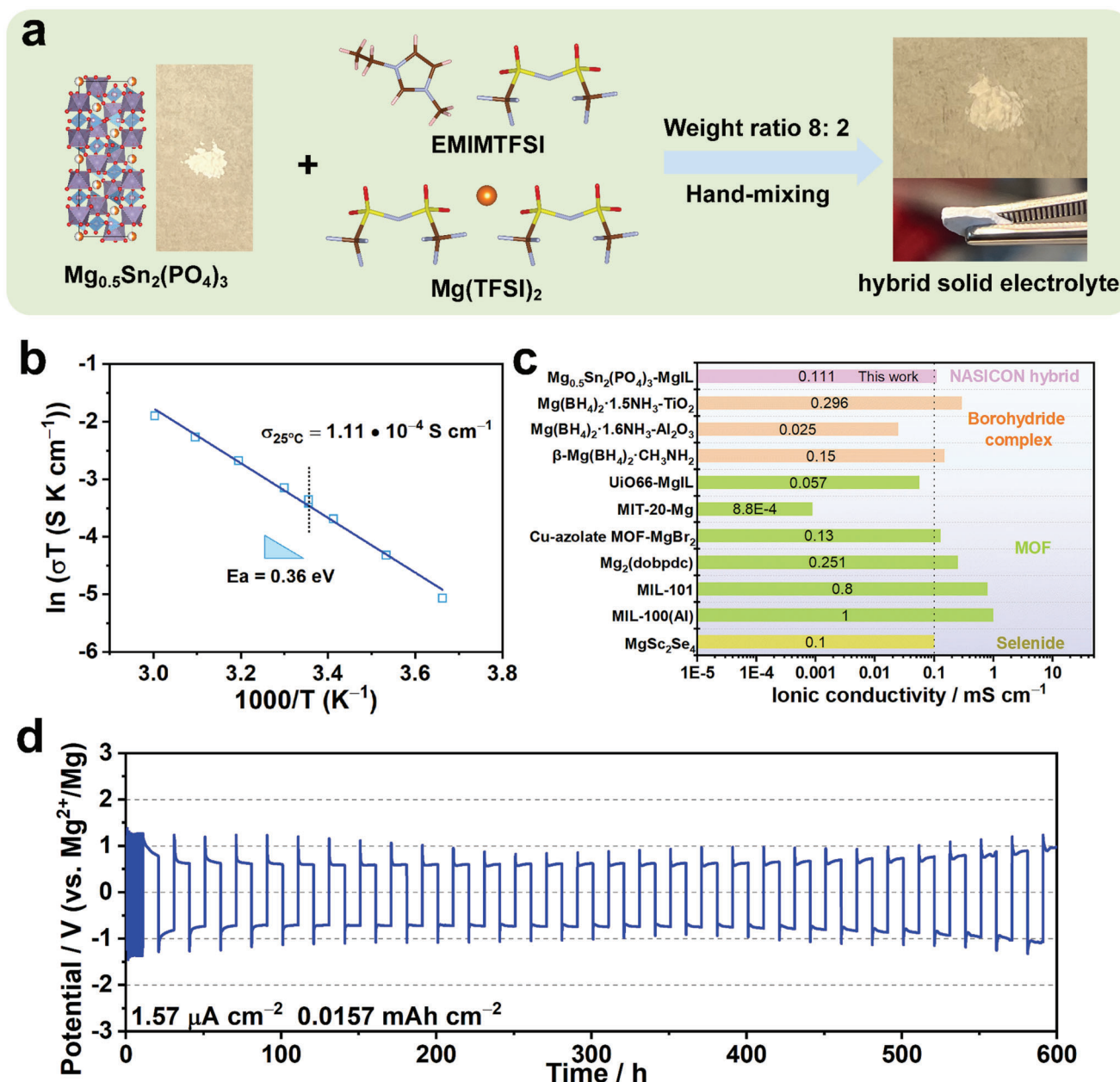


**Figure 3.** a) Schematic illustration of the preparation of MgSP-HSE; b) Arrhenius plot of MgSP-HSE; c) room-temperature ionic conductivity comparison of state-of-the-art Mg-ion conductors,<sup>[31–39]</sup> the dashed line marks the ionic conductivity of  $1 \times 10^{-4} \text{ S cm}^{-1}$ ; d) potential profile of Mg plating–stripping at current density of  $1.57 \mu\text{A cm}^{-2}$ .

require higher conductivities.<sup>[40]</sup> After infiltration of the ionic liquid, the as-prepared HSE shows satisfactory ionic conductivity comparable with MOF-based materials and borohydride complexes, which are the only two groups of electrolyte materials for (almost) solid Mg batteries that can reach the  $10^{-4} \text{ S cm}^{-1}$  scale of ionic conductivity so far, except for the inorganic  $\text{MgSc}_2\text{Se}_4$  spinel, as listed in Figure 3c. Encouragingly, the oxidation stability of the MgSP-HSE reaches 3.3 V versus  $\text{Mg}^{2+}/\text{Mg}$  in linear scan voltammetry (LSV) measurements (Figure S6, Supporting Information), much higher compared to the Mg borohydrides which are 1.2 V,<sup>[31–33]</sup> largely expanding the choice of cathode ma-

terial candidates. In addition, as shown here to the best of our knowledge for the first time, the MgSP-HSE allows reversible Mg plating and stripping in an “almost solid” symmetric cell system at room temperature. As shown in Figure 3d, symmetric cells using Mg foils as both working and counter electrodes were assembled. Initially, the symmetric cells were activated by charging and discharge for 10 cycles at a current density of  $1.57 \mu\text{A cm}^{-2}$  with alternating plating and stripping times of 30 min for each step (plated charge amount of  $0.785 \mu\text{Ah cm}^{-2}$ , corresponding to 2 nm of Mg assuming homogeneous plating–stripping). Afterward, the plated charge was increased to  $0.0157 \text{ mAh cm}^{-2}$ ,

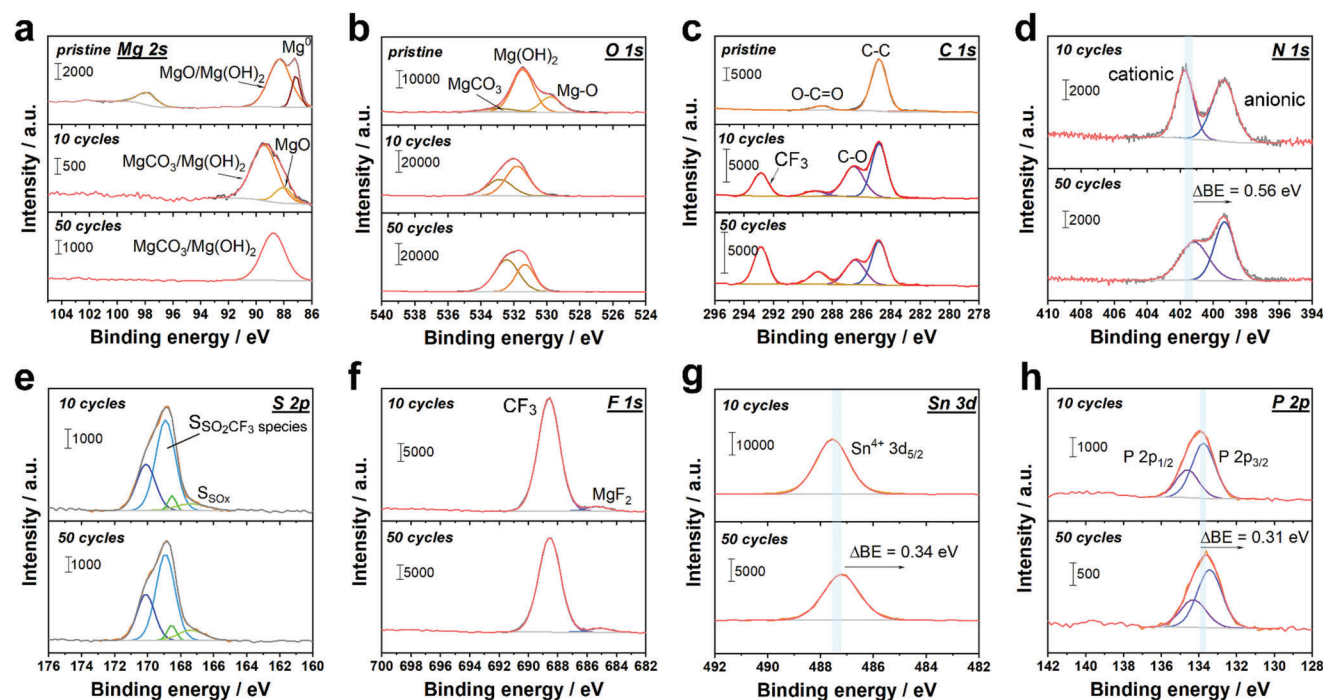


**Figure 4.** X-ray photoelectron spectra of a) Mg 2s; b) O 1s; c) C 1s; d) N 1s; e) S 2p; f) F 1s; g) Sn 3d and h) P 2p signals of pristine Mg foil and Mg foils after 10 and 50 cycles.

corresponding to 10 h (and 41 nm of magnesium) for each step, where the Mg plating–stripping process demonstrates a stable deposition overpotential of 0.6 V versus  $\text{Mg}^{2+}/\text{Mg}$  for over 500 hours.

## 2.4. Surface Analysis

To figure out the composition and evolution of the HSE-derived interface between Mg and HSE, X-ray photoelectron spectroscopy (XPS) characterization was carried out. XP spectra of the pristine Mg foil and the Mg foils after cycling for 10 cycles and 50 cycles in a symmetric cell setup at  $0.0157 \text{ mA h cm}^{-2}$  are shown in **Figure 4**. First of all, the Mg foil surface was analyzed after peeling off the surface oxide layer. As shown in Figure 4a,b, even after careful polishing, the Mg foil surface still contains a considerable amount of passivation film containing MgO and  $\text{Mg}(\text{OH})_2$ .<sup>[41,42]</sup> This could be attributed to the strong affinity of Mg with oxygen, as well as trace amounts of water absorbed on the surface, respectively. However, the binding energies of the two compounds are too close to be deconvoluted. Other than that, there is also a hint of  $\text{MgCO}_3$  on the surface, which is suggested by the O–C=O signal in the O 1s and C 1s spectra (Figure 4c).<sup>[43]</sup> After the cycling experiments, the MgO content gradually decreased, resulting in  $\text{Mg}(\text{OH})_2$  and  $\text{MgCO}_3$  becoming the primary Mg-containing components of the interphase. The relative ratio between these two compounds exhibits dynamic behavior. This is also supported by the depth profiling XP spectra. As shown in Figure S7b (Supporting Information), after etching the Mg foil (after 50 cycles) by argon ion sputtering, the relative intensity of  $\text{MgCO}_3$  decreases while that of  $\text{Mg}(\text{OH})_2$  increases, un-

til the pristine foil surface is reached, as suggested by the sharp intensity increase of MgO (Figure S7a, Supporting Information) and decrease of C–C bond (Figure S7c, Supporting Information). The trend correlates well with the spectra in Figure 4b, suggesting that upon cycling, the SEI demonstrates a graded composition, where  $\text{Mg}(\text{OH})_2$  component dominates the nearest layer on the Mg foil, while the  $\text{MgCO}_3$  component dominates the second.

The interface also contains TFSI<sup>−</sup> residuals from the HSE, as suggested in the C 1s, N 1s, S 2p, and F 1s signals (Figure 4c–f).<sup>[44,45]</sup> Surprisingly, the binding energies of  $\text{C}_{\text{TFSI}}$  (–CF<sub>3</sub>),  $\text{N}_{\text{TFSI}}$  (anionic),  $\text{F}_{\text{TFSI}}$  (–CF<sub>3</sub>), and  $\text{S}_{\text{TFSI}}$  (–SO<sub>2</sub>CF<sub>3</sub>) peaks all remain unchanged comparing the Mg foil after 10 cycles with the one after 50 cycles. This suggests the superior chemical and electrochemical stability of the TFSI<sup>−</sup> anion during the Mg plating–stripping. It is worth noting that an unexpected signal at  $E_{\text{B}} = 685.3 \text{ eV}$  is observed on the surface of cycled Mg foils, which can be attributed to  $\text{MgF}_2$ .<sup>[45]</sup> However, we assume that this is due to the instability of the TFSI<sup>−</sup> anion under X-ray radiation,<sup>[46]</sup> instead of the electrochemical degradation of TFSI<sup>−</sup> anion during cycling. As shown in Figure S8a (Supporting Information), the signal of  $\text{MgF}_2$  is initially absent in the  $\text{Mg}(\text{TFSI})_2$  powder. Nevertheless, upon continuous X-ray exposure, the TFSI<sup>−</sup> anion starts to decompose, as suggested by the increased intensity of  $\text{MgF}_2$  peak and decreased intensity of CF<sub>3</sub> peak. The same trend is observed in the F 1s XP spectra of the MgSP–MgIL electrolyte powder (Figure S8b, Supporting Information). However, since the percentage of MgIL is small in the HSE (20 wt.%), the peak intensity of  $\text{MgF}_2$  is comparably small compared to the pure  $\text{Mg}(\text{TFSI})_2$  salt. Further evidence is that the  $\text{MgF}_2$  signal was not observed on the surface of Mg foils after cycling when the number of measurement scans was kept to a



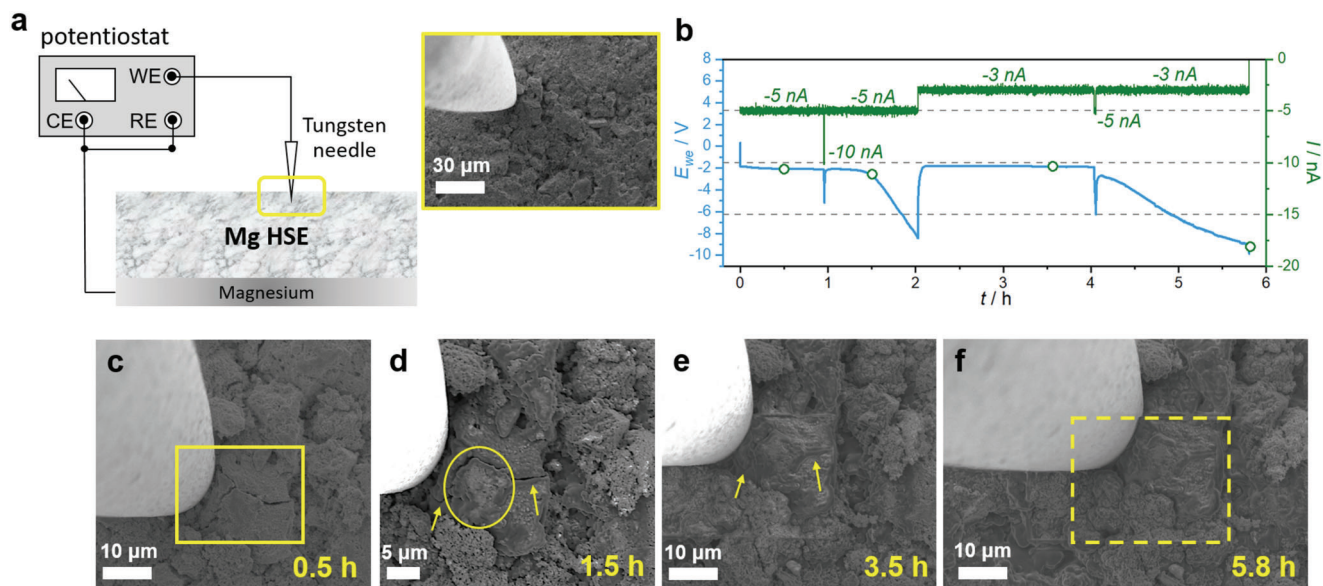


**Figure 5.** a) Schematic illustration for the setup of in situ SEM, adapted based on previous work.<sup>[28]</sup> The inset shows the initial morphology of MgSP-HSE; b) potential profile with different applied currents during the Mg deposition; c–f) top-view SEM images of the solid-state micro-cell after different plating times marked in (b).

minimum to reduce the radiation damage (see Figure S9, Supporting Information).<sup>[47]</sup> Additionally, the absence of sulfide signals in the S 2p spectrum (Figure 4e) agrees well with the stability of the TFSI<sup>-</sup> anion.<sup>[45,48]</sup> In contrast, the signal of the EMIM<sup>+</sup> cation shifts to a lower binding energy by 0.56 eV, indicating the possible reduction of the radical cation. Furthermore, we also looked into the spectra of the Mg<sub>0.5</sub>Sn<sub>2</sub>(PO<sub>4</sub>)<sub>3</sub>. As shown in Figure 4g, the peak of Sn 3d<sub>5/2</sub> is located at  $E_b = 487.55$  eV, which can be indexed to Sn<sup>4+</sup>.<sup>[49]</sup> This suggests the stability of Mg<sub>0.5</sub>Sn<sub>2</sub>(PO<sub>4</sub>)<sub>3</sub> in the HSE, yet with a small degree of partial reduction due to the formation of an interphase, indicated by the binding energy shift toward a lower value by 0.34 eV. We note, that the small binding energy change cannot be attributed to full reduction to Sn<sup>2+</sup> from Sn<sup>4+</sup>, as the binding energy difference of the two valence states ought to fall between 0.7 eV and 1.1 eV.<sup>[49–52]</sup> The same trend is observed in the P 2p signal (Figure 4h), where the doublet peaks also shift to a lower binding energy by 0.31 eV. In summary, XPS suggests that the HSE is well-compatible with the Mg metal anode and that the interface is relatively stable. This stability allows for stable repetitive Mg plating and stripping at room temperature. However, the low Mg-ion conductivity of the interphase components dominated by MgCO<sub>3</sub> and Mg(OH)<sub>2</sub> contributes to the high Mg plating–stripping overpotential, which will be the future key issue to be solved through surface modification.

## 2.5. In Situ Electrochemical-Scanning Electron Microscopy (SEM) Studies

As discussed above, although the room-temperature ionic conductivity of the HSE is satisfactory, it is the HSE|Mg interface that contributes significantly to the overall impedance in the Mg SSBs. Apart from the interphase formed chemically, the

work-hardened magnesium foil along with its hexagonal lattice structure leads to poor interfacial contact even at high pressure (300 MPa). Specifically, the Young's modulus of magnesium is 45 GPa, nine times higher compared to lithium (4.9 GPa).<sup>[53]</sup> More importantly, the yield strength of magnesium also exceeds that of lithium to a large extent ( $\approx 100$  MPa vs 16 MPa).<sup>[54,55]</sup> This leads to a significant overpotential for Mg deposition even at low current densities, resulting in experimental difficulties in studying such systems in a pouch cell setup. Such an interfacial-dominating process gives rise to sluggish Mg deposition, in consequence, identifying and studying the properties of deposited Mg on a substrate in ex situ characterization techniques can be fairly challenging. In this regard, in situ electrochemical SEM measurements were performed to get more fundamental insights into Mg growth inside SSB, wherein Mg was deposited at a tungsten microneedle. The cell setup is illustrated in Figure 5a. Briefly, a free-standing, isostatically pressed (300 MPa) MgSP-HSE pellet (thickness of  $\approx 1$  mm, diameter of 1 cm) was fixed to a magnesium foil (thickness of 100  $\mu$ m, diameter of 9 mm) with well-polished surface, that was used as Mg reservoir and reference electrode. On the other hand, the tungsten needle, as shown in Figure 5a, operated by motors was used as current collector for Mg deposition due to the chemical stability of Mg against W.<sup>[56]</sup> The cathodic deposition of Mg at tungsten microneedle was performed by varying the current (Figure 5b). As can be seen, the deposition at  $-5$  nA requires an overpotential of  $\approx -1.9$  V. This can be attributed to the constriction resistance at the small Mg|MgSP-HSE interface and the resulting  $iR$  drop. The cell overpotential continuously increases during the deposition, e.g., an overpotential of  $-8.5$  V was reached at  $\approx 2$  h. We attribute this to the progressively depleting contact at the anodic (reservoir) interface. To overcome this, the local pressure was increased via the tungsten microneedle to facilitate contact at Mg|MgSP-HSE interface. The inset in Figure 5a shows an SEM image of the

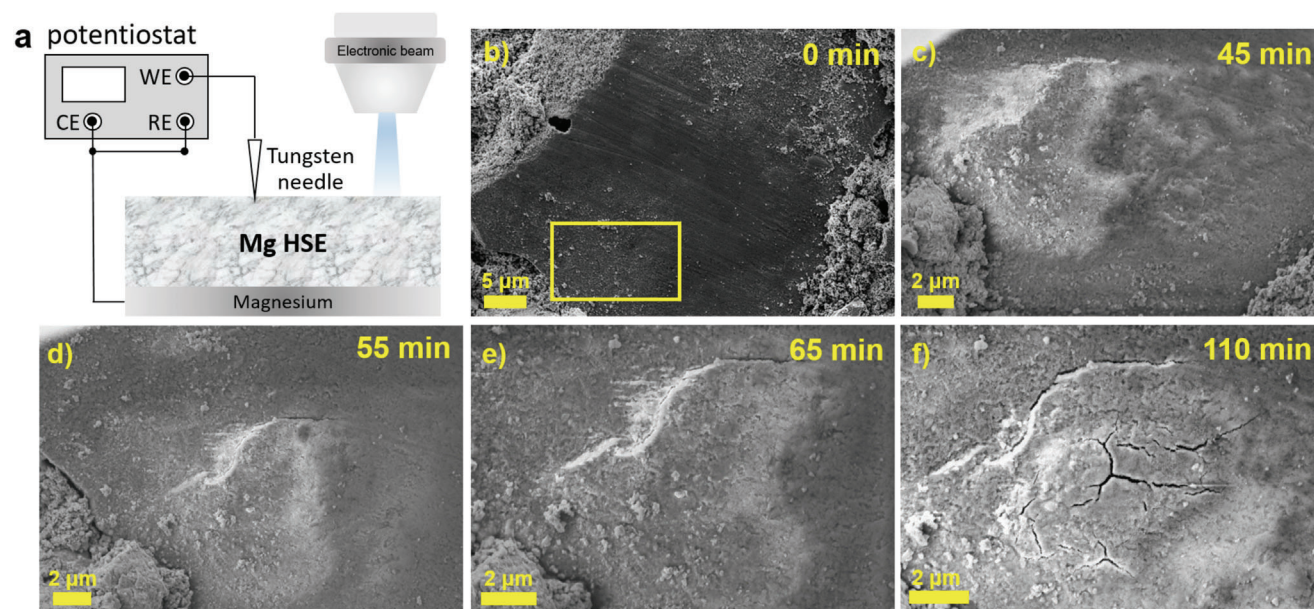


**Figure 6.** a) Schematic illustration for the setup of in situ SEM; b–f) Top-view SEM images of the MgSP-HSE after injecting electrons for different time durations.

contact spot before plating. We note that the contact spot has been pre-deposited for  $\approx 20$  s during the attempt to drive a higher current through the contact (Figure S10, Supporting Information). Galvanostatic deposition leads to Mg deposition, as indicated in Figure 5d. From this spot, further plating leads to lateral and conformal growth of magnesium to gradually cover the crack (arrows for comparison in Figure 5d,e) before the significant overpotential increase ( $\approx -9$  V) at  $\approx 4$  h. Figure 5f shows the final state of the selected area after deposition for  $\approx 6$  h according to the shown galvanostatic profile (Figure 5b). The SEM image of the deposited spot obtained after tungsten microneedle removal indicates the deposition of an Mg thin film (Figure S11, Supporting Information). Also, as can be seen in Figure 5b, changing the applied current during the plating did not impact the morphology of the plated magnesium. However, sudden current increase may give rise to rapid voltage drop (see example at  $\approx 1$  h where the current was increased from  $-5$  nA to  $-10$  nA). To figure out the parameters affecting the Mg growth behavior such as current at different applied pressures, follow-up work is underway.

Moreover, we performed experiments wherein the deposition was performed on a single SE particle. In this scenario, the tungsten needle is also connected to top of the MgSP-HSE pellet (Figure 6a). Here, the SEM electron beam (2 nA for 110 min), as a virtual electrode, was used for  $\text{Mg}^{2+}$  reduction, while the tungsten needle was positioned at a close area to mediate contact at the other side. Figure 6b shows the target area before beam irradiation. As shown in Figure 6c, after 45 min, a bump can be observed, which induced cracking on the edge of the plated area within the next 20 min (Figure 6d,e). Afterward, instead of forming other nucleation spots on the edge out of crack, the reduced  $\text{Mg}^0$  continues to grow underneath (see EDX images in Figure S12, Supporting Information), and eventually stimulates more cracks on top of the particle (Figure 6f), adding evidence of

the room temperature Mg-ion conduction of the designed solid-electrolyte.

### 3. Conclusion

In summary, we report a new NASICON-type material  $\text{Mg}_{0.5}\text{Sn}_2(\text{PO}_4)_3$  which shows room temperature Mg-ion conductivity in the range of  $10^{-9}$  S  $\text{cm}^{-1}$ . After impregnating the SE particles with 20 wt.% of ionic liquid, the room temperature conductivity of the hybrid solid electrolyte reaches  $\sigma(\text{Mg}^{2+}) = 1.11 \times 10^{-4}$  S  $\text{cm}^{-1}$ , with a low activation energy of 0.36 eV. Reversible and stable Mg plating–stripping at ambient temperature was realized by using the HSE. Surface analysis suggests good compatibility of the electrolyte with the Mg metal anode. In addition, the Mg plating was observed for the first time via an in situ SEM technique, which shows a planar growth behavior. The presented results contribute to the understanding of Mg growth in solid-state batteries and hold great promise for further development of the Mg metal anode.

### 4. Experimental Section

**Materials:** Citric acid [Acros Organics, 99%],  $\text{Mg}(\text{CH}_3\text{COO})_2 \cdot 4\text{H}_2\text{O}$  [Alfa Aesar, 98%],  $\text{SnCl}_2$  [Sigma Aldrich, 98%],  $\text{NH}_4\text{H}_2\text{PO}_4$  [Alfa Aesar], Magnesium bis (trifluoromethanesulfonyl) imide [ $\text{Mg}(\text{TFSI})_2$ , TCI, >97%], 1-ethyl-3-methylimidazolium bis (trifluoromethanesulfonyl) imide ([EMIM][TFSI], TCI, >98%), Mg foil [ChemPUR 99.98%],  $\text{Al}_2\text{O}_3$  [Sigma-Aldrich].

**Synthesis of  $\text{Mg}_{0.5}\text{Sn}_2(\text{PO}_4)_3$ :**  $\text{Mg}_{0.5}\text{Sn}_2(\text{PO}_4)_3$  was prepared by a sol-gel method. Typically, citric acid (1.9213 g, 10 mmol) as chelating agent was added into distilled water (150 mL) until fully dissolved.  $\text{Mg}(\text{CH}_3\text{COO})_2$  (0.4289 g, 2 mmol),  $\text{SnCl}_2$  (1.5169 g, 8 mmol),  $\text{NH}_4\text{H}_2\text{PO}_4$  (1.3804 g, 12 mmol) with molar ratio of 1:4:6 were added to the citric acid solution during continuous magnetic stirring. After stirring for 2 h, the solution was heated up to 90 °C under an oil bath until the



water got totally vaporized. Then, the solid product was collected and ground into powder. Subsequently, the powder was sintered at 500 °C for 6 h and at 750 °C for 6 h, respectively, with intermediate grinding. The final white powder was then obtained after sintering at 800 °C for 12 h.

**Preparation of Hybrid Solid Electrolyte:** The preparation of hybrid solid electrolytes was carried out in an Argon-filled glovebox. Firstly, the Mg(TFSI)<sub>2</sub> powder was dried at 150 °C for 24 h under vacuum before use, which was then dissolved in [EMIM][TFSI] ionic liquid with a concentration of 1 M at 100 °C. After the powder was completely dissolved, the transparent ionic liquid solution was cooled down to room temperature before use. Afterward, the hybrid solid electrolyte powder was obtained by mixing the Mg<sub>0.5</sub>Sn<sub>2</sub>(PO<sub>4</sub>)<sub>3</sub> powder and the above magnesium ionic liquid with different weight ratios through hand-milling in an agate mortar for 20 min and aged at 60 °C for 4 h. For the control experiment, Al<sub>2</sub>O<sub>3</sub> was mixed with IL with weight ratio of 8:2 at the same condition.

**Material Characterization:** The powder X-ray diffraction (XRD) patterns were collected on an Empyrean powder diffractometer (Malvern Panalytical Ltd) using Cu K<sub>α</sub> radiation (λ<sub>1</sub> = 1.5405980 Å; λ<sub>2</sub> = 1.5444260 Å) in reflection geometry. Data were recorded in the 2θ range from 10° to 80° with a step size of 0.013° or 0.026°. Rietveld refinement of the powder XRD pattern was carried out with Fullprof software. The reference structural information such as atomic position was derived from two NASICON-structured materials, Mg<sub>0.5</sub>Ti<sub>2</sub>(PO<sub>4</sub>)<sub>3</sub> (JCPDS #43-0073) and NaSn<sub>2</sub>(PO<sub>4</sub>)<sub>3</sub> (JCPDS #49-1198). Crystal structure illustration was obtained from VESTA software. Scanning electron microscopy images (SEM) of the powder samples were obtained with a Zeiss Merlin instrument at an acceleration voltage of 3 kV. X-ray photoelectron spectroscopy (XPS) was performed on a PHI VersaProbe 4 Scanning ESCA Microprobe (Physical Electronics) with a monochromatized Al K<sub>α</sub> source (1486.6 eV). The X-ray was set to the 100 W high power setting which scans a 100 μm spot over a 1400 μm wide area, thus averaging the signal over a larger area. For deeper analysis of the F 1s detailed spectra, the X-ray power and beam diameter were set to 50 W and 200 μm, respectively. The samples were mounted on insulating tape and transferred from an Ar-filled glovebox to the XPS instrument chamber using an Ar-filled transfer module. The PHI dual beam charge neutralization consisting of a low current of 10 eV Ar<sup>+</sup> ions and a higher current of ±2 eV electrons was employed during measurement. The detail spectra were taken with a pass energy of 27 eV and a step size of 0.2 eV. For N 1s the pass energy was set to 55 eV to compensate for the low concentration. For XPS depth profiling, a sputter gun with Ar<sup>+</sup> ions (acceleration voltage ranges from 0.5 kV to 4 kV) was used for a sputtered area of 3 × 3 mm<sup>2</sup>. CasaXPS software was used to analyze the XPS data, where Shirley-type background correction was applied. Before fitting, all the peaks were calibrated with respect to the adventitious carbon (284.8 eV).

**Electrochemical Measurements:** The electrochemical measurements were performed with a VMP300 electrochemical workstation from Bio-Logic Science Instruments SAS. For ionic conductivity measurements, a two-electrode home-designed battery cell casing was used. In a typical measurement, 80 mg Mg<sub>0.5</sub>Sn<sub>2</sub>(PO<sub>4</sub>)<sub>3</sub> or HSE powder was filled in the PEEK housing with a diameter of 10 mm. Stainless steel stamps were employed as blocking electrodes. The symmetric cell was then pressed at 3 tons for 3 min where electrolyte pellets form inside the PEEK housing. The electrochemical impedance measurements were carried out in the frequency range from 3 MHz – 100 mHz by applying a 100 mV or 10 mV amplitude voltage for Mg<sub>0.5</sub>Sn<sub>2</sub>(PO<sub>4</sub>)<sub>3</sub> and MgSP-HSE, respectively. Ionic conductivities were calculated based on the following equation:

$$\sigma = \frac{1}{R} \cdot \frac{l}{A} \quad (1)$$

where *R* is the resistance obtained from fitted result (RelaxIS 3 software, RHD Instruments, Darmstadt, Germany) from Nyquist plots, while *l* and *A* represent the thickness and area of the electrolyte pellet, respectively. For temperature dependence measurements, a climate chamber (Weisstechnik) was used. Impedance spectra were recorded at different temperatures between 0 °C and 60 °C after being kept at a certain tempera-

ture for 1.5 h. The activation energy (*E<sub>A</sub>*) was determined according to the Arrhenius equation:

$$\sigma = \frac{\sigma_0}{T} \exp\left(-\frac{E_A}{k_B T}\right) \quad (2)$$

with σ<sub>0</sub> being the conductivity prefactor. For the Mg plating–stripping measurements, the HSE pellet was first pressed in the same way as the procedures above. Then, Mg foils (Ø = 9 mm) polished with a scalpel were put on both sides of the HSE pellet. Afterward, the cell was again pressed at 3 tons for 1 min. During the electrochemical measurements, a constant pressure was applied on the cells by using the screw of aluminum framework with 10 N m torque.

**Density-Functional Theory Calculation:** The properties of the Mg<sub>0.5</sub>Sn<sub>2</sub>(PO<sub>4</sub>)<sub>3</sub> were studied using periodic density functional theory (DFT),<sup>[57–59]</sup> as implemented in the Vienna Ab initio Simulation Package.<sup>[60–62]</sup> To account for exchange and correlation the generalized gradient approximation in the formulation of Perdew, Burke, and Ernzerhof (PBE)<sup>[63]</sup> was used. The electron-core interactions were represented by the Projector Augmented Wave (PAW)<sup>[64]</sup> method. Calculations were performed with the Brillouin zone sampled using a 4 × 4 × 1 k-point grid in an *a* = *b* = 8.80 Å and *c* = 21.42 Å unit cell containing six formula units. The electronic structure was converged to 1 × 10<sup>−5</sup> eV, applying a plane-wave cutoff energy of 550 eV. All formation energies with respect to the insertion of the Mg atoms were determined with respect to the Mg metal bulk energy with *E<sub>n</sub>* and *E<sub>n−1</sub>* being the energies of Mg<sub>*n*</sub>Sn<sub>18</sub>(PO<sub>4</sub>)<sub>24</sub>:

$$E_{\text{form}} = E_n - E_{n-1} - E_{\text{Mg}} \quad (3)$$

$$E_{\text{form}} = E_n - n \cdot E_{\text{Mg}} \quad (4)$$

$$E_{\text{volt}} = -\frac{E_n - E_{n-1} - E_{\text{Mg}}}{2} \quad (5)$$

The migration barriers for bulk diffusion were obtained by applying the climbing image Nudged Elastic Band (NEB) method.<sup>[65]</sup> The calculations were performed using three distinct images along the pathway toward the meta-stable intermediate and then mirroring the path to get a full diffusion event, while all forces on the atoms converged within 0.08 eV Å<sup>−1</sup>.

**In Situ SEM Measurements:** To prepare the solid-state cell inside the SEM chamber, an HSE pellet (diameter of 10 mm, thickness of ≈1 mm) was first prepared via isostatic press. Then, the pellet was fixed on top of a magnesium metal foil with a well-polished surface that was used as an Mg-reservoir and reference electrode, which was attached to a copper tape on the sample holder; on the other side of HSE pellet, a tungsten needle operated by a micromanipulator (prober module, Kamrath & Weiss GmbH) was connected. To avoid air contamination, the samples were transferred from the Ar-filled glovebox to SEM chamber via a Leica transfer module (EM VCT 500). By driving current via a potentiostat (Bio-Logic, VMP200), the tungsten needle could act as micro working electrode for the reduction spot of Mg<sup>2+</sup>. At different states of charge, SEM pictures were taken at an acceleration voltage of 4 kV. When using an electron beam from the SEM column to inject electrons, the current was set to 2 nA.

## Supporting Information

Supporting Information is available from the Wiley Online Library or from the author.

## Acknowledgements

This work was funded by the German Research Foundation (DFG) under Project ID 390874152 (POLiS Cluster of Excellence). The financial support from the Federal Ministry of Education and Research (BMBF) within the FestBatt II project (03XP0433D) was also acknowledged. The authors

would like to thank Prof. Helmut Ehrenberg (Karlsruhe Institute of Technology) for the valuable discussion on XRD results. The authors also thank experimental support by Dr. Boris Mogwitz and Dr. Klaus Peppler (JLU Giessen).

Open access funding enabled and organized by Projekt DEAL.

## Conflict of Interest

The authors declare no conflict of interest.

## Data Availability Statement

The data that support the findings of this study are openly available in Zenodo at <https://doi.org/10.5281/zenodo.8338560>, reference number 8338560.

## Keywords

hybrid solid electrolytes, ionic liquids, magnesium batteries, magnesium deposition, NASICONs, solid electrolytes

Received: August 3, 2023

Revised: September 14, 2023

Published online: October 10, 2023

- [1] Z. W. B. Iton, K. A. See, *Chem. Mater.* **2022**, *34*, 881.
- [2] J. D. Forero-Saboya, D. S. Tchitchekova, P. Johansson, M. R. Palacín, A. Ponrouch, *Adv. Mater. Interfaces* **2022**, *9*, 2101578.
- [3] L. E. Blanc, D. Kundu, L. F. Nazar, *Joule* **2020**, *4*, 771.
- [4] Y. Liang, H. Dong, D. Aurbach, Y. Yao, *Nat. Energy* **2020**, *5*, 646.
- [5] K. W. Leong, W. Pan, X. Yi, S. Luo, X. Zhao, Y. Zhang, Y. Wang, J. Mao, Y. Chen, J. Xuan, H. Wang, D. Y. C. Leung, *Sci. Adv.* **2023**, *9*, eadh1181.
- [6] D. Aurbach, Z. Lu, A. Schechter, Y. Gofer, H. Gizbar, R. Turgeman, Y. Cohen, M. Moshkovich, E. Levi, *Nature* **2000**, *407*, 724.
- [7] J. Eaves-Rathert, K. Moyer, M. Zohair, C. L. Pint, *Joule* **2020**, *4*, 1324.
- [8] R. Davidson, A. Verma, D. Santos, F. Hao, C. D. Fincher, D. Zhao, V. Attari, P. Schofield, J. Van Buskirk, A. Fraticelli-Cartagena, T. E. G. Alivio, R. Arroyave, K. Xie, M. Pharr, P. P. Mukherjee, S. Banerjee, *Mater. Horiz.* **2019**, *7*, 843.
- [9] Z. Song, Z. Zhang, A. Du, S. Dong, G. Li, G. Cui, *Adv. Mater.* **2021**, *33*, 2100224.
- [10] S.-B. Son, T. Gao, S. P. Harvey, K. X. Steirer, A. Stokes, A. Norman, C. Wang, A. Cresce, K. Xu, C. Ban, *Nat. Chem.* **2018**, *10*, 532.
- [11] T. Famprakis, P. Canepa, J. A. Dawson, M. S. Islam, C. Masquelier, *Nat. Mater.* **2019**, *18*, 1278.
- [12] T. Krauskopf, F. H. Richter, W. G. Zeier, J. Janek, *Chem. Rev.* **2020**, *120*, 7745.
- [13] Y. Lu, L. Li, Q. Zhang, Z. Niu, J. Chen, *Joule* **2018**, *2*, 1747.
- [14] S. Ikeda, M. Takahashi, J. Ishikawa, K. Ito, *Solid State Ionics* **1987**, *23*, 125.
- [15] N. K. Anuar, N. S. Mohamed, *J. Sol-gel Sci. Techn.* **2016**, *80*, 249.
- [16] N. K. Anuar, S. B. R. S. Adnan, M. H. Jaafar, N. S. Mohamed, *Ionics* **2016**, *22*, 1125.
- [17] K. Nakano, Y. Noda, N. Tanibata, M. Nakayama, K. Kajihara, K. Kanamura, *RSC Adv.* **2019**, *9*, 12590.
- [18] S. Tamura, M. Yamane, Y. Hoshino, N. Imanaka, *J. Solid State Chem.* **2016**, *235*, 7.
- [19] A. Paoletta, G. Bertoni, W. Zhu, D. Campanella, A. La Monaca, G. Girard, H. Demers, A. C. Gheorghe Nita, Z. Feng, A. Vijh, A. Guerfi, M. Trudeau, M. Armand, S. A. Krachkovskiy, *J. Am. Chem. Soc.* **2022**, *144*, 3442.
- [20] Z. Chang, H. Yang, X. Zhu, P. He, H. Zhou, *Nat. Commun.* **2022**, *13*, 1510.
- [21] M. Watanabe, M. L. Thomas, S. Zhang, K. Ueno, T. Yasuda, K. Dokko, *Chem. Rev.* **2017**, *117*, 7190.
- [22] J. Hwang, K. Matsumoto, C.-Y. Chen, R. Hagiwara, *Energy Environ. Sci.* **2021**, *14*, 5834.
- [23] S. A. Pervez, B. P. Vinayan, M. A. Cambaz, G. Melinte, T. Diemant, T. Braun, G. Karkera, R. J. Behm, M. Fichtner, *J. Mater. Chem. A* **2020**, *8*, 16451.
- [24] S. A. Pervez, G. Kim, B. P. Vinayan, M. A. Cambaz, M. Kuenzel, M. Hekmatfar, M. Fichtner, S. Passerini, *Small* **2020**, *16*, 2000279.
- [25] S. Xiong, Y. Liu, P. Jankowski, Q. Liu, F. Nitze, K. Xie, J. Song, A. Matic, *Adv. Funct. Mater.* **2020**, *30*, 2001444.
- [26] D. Safanama, S. Adams, *J. Power Sources* **2017**, *340*, 294.
- [27] W. D. Richards, L. J. Miara, Y. Wang, J. C. Kim, G. Ceder, *Chem. Mater.* **2016**, *28*, 266.
- [28] T. Krauskopf, B. Mogwitz, H. Hartmann, D. K. Singh, W. G. Zeier, J. Janek, *Adv. Energy Mater.* **2020**, *10*, 2000945.
- [29] Q. Wang, H. Gao, J. Li, G.-B. Liu, H. Jin, *ACS Appl. Mater. Interfaces* **2021**, *13*, 14312.
- [30] M. Avdeev, *Chem. Mater.* **2021**, *33*, 7620.
- [31] Y. Yan, J. B. Grinderslev, T. Burankova, S. Wei, J. P. Embs, J. Skibsted, T. R. Jensen, *J. Phys. Chem. Lett.* **2022**, *13*, 2211.
- [32] Q. Wang, H. Li, R. Zhang, Z. Liu, H. Deng, W. Cen, Y. Yan, Y. Chen, *Energy Storage Mater.* **2022**, *51*, 630.
- [33] M. B. Amdisen, J. B. Grinderslev, L. N. Skov, T. R. Jensen, *Chem. Mater.* **2023**, *35*, 1440.
- [34] P. Canepa, S.-H. Bo, G. Sai Gautam, B. Key, W. D. Richards, T. Shi, Y. Tian, Y. Wang, J. Li, G. Ceder, *Nat. Commun.* **2017**, *8*, 1759.
- [35] S. Ma, L. i Shen, Q. Liu, W. Shi, C. Zhang, F. Liu, J. A. Baucom, D. Zhang, H. Yue, H. B. Wu, Y. Lu, *ACS Appl. Mater. Interfaces* **2020**, *12*, 43824.
- [36] Y. Yoshida, T. Yamada, Y. Jing, T. Toyao, K.-I. Shimizu, M. Sadakiyo, *J. Am. Chem. Soc.* **2022**, *144*, 8669.
- [37] M. L. Aubrey, R. Ameloot, B. M. Wiers, J. R. Long, *Energy Environ. Sci.* **2013**, *7*, 667.
- [38] S. S. Park, Y. Tulchinsky, M. Dinca, *J. Am. Chem. Soc.* **2017**, *139*, 13260.
- [39] Z. Wei, R. Maile, L. M. Riegger, M. Rohnke, K. Müller-Buschbaum, J. Janek, *Batter. Supercaps* **2022**, *5*, e202200318.
- [40] J. Janek, W. G. Zeier, *Nat. Energy* **2023**, *8*, 230.
- [41] H. B. Yao, Y. Li, A. T. S. Wee, *Appl. Surf. Sci.* **2000**, *158*, 112.
- [42] S. Ardizzone, C. L. Bianchi, M. Fadoni, B. Vercelli, *Appl. Surf. Sci.* **1997**, *119*, 253.
- [43] M. Chen, W. Hua, J. Xiao, D. Cortie, W. Chen, E. Wang, Z. Hu, Q. Gu, X. Wang, S. Indris, S.-L. Chou, S.-X. Dou, *Nat. Commun.* **2019**, *10*, 1480.
- [44] I. Weber, J. Kim, F. Buchner, J. Schnaidt, R. J. Behm, *ChemSusChem* **2020**, *13*, 2589.
- [45] Y. He, Q. i Li, L. Yang, C. Yang, D. Xu, *Angew. Chem.* **2019**, *131*, 7697.
- [46] I. Shterenberg, M. Salama, Y. Gofer, D. Aurbach, *J. Phys. Chem. C* **2017**, *121*, 3744.
- [47] S. Malmgren, K. Ciosek, R. Lindblad, S. Plogmaker, J. Kühn, H. Rensmo, K. Edström, M. Hahlin, *Electrochim. Acta* **2013**, *105*, 83.
- [48] M. S. Ding, T. Diemant, R. J. Behm, S. Passerini, G. A. Giffin, *J. Electrochem. Soc.* **2018**, *165*, A1983.
- [49] M. Liao, B.-B. Yu, Z. Jin, W. Chen, Y. Zhu, X. Zhang, W. Yao, T. Duan, I. Djerdj, Z. He, *ChemSusChem* **2019**, *12*, 5007.
- [50] F. Li, Y. Xie, Y. Hu, M. Long, Y. Zhang, J. Xu, M. Qin, X. Lu, M. Liu, *ACS Energy Lett.* **2020**, *5*, 1422.
- [51] Y. Liao, H. Liu, W. Zhou, D. Yang, Y. Shang, Z. Shi, B. Li, X. Jiang, L. Zhang, L. i N. a Quan, R. Quintero-Bermudez, B. R. Sutherland, Q. Mi, E. H. Sargent, Z. Ning, *J. Am. Chem. Soc.* **2017**, *139*, 6693.
- [52] F. Lu, X. Ji, Y. Yang, W. Deng, C. E. Banks, *RSC Adv.* **2013**, *3*, 18791.

- [53] G. V. Samsonov, *Handbook of the physicochemical properties of the elements*, Springer, New York **1968**, 387.
- [54] X. Zhang, Q. J. Wang, K. L. Harrison, S. A. Roberts, S. J. Harris, *Cell Reports Physical Science* **2020**, *1*, 100012.
- [55] W. Xu, N. Birbilis, G. Sha, Yu Wang, J. E. Daniels, Y. Xiao, M. Ferry, *Nat. Mater.* **2015**, *14*, 1229.
- [56] S. Terlicka, P. Darlak, N. Sobczak, J. J. Sobczak, *Materials* **2022**, *15*, 9024.
- [57] P. Hohenberg, W. Kohn, *Phys. Rev.* **1964**, *136*, B864.
- [58] W. Kohn, L. J. Sham, *Phys. Rev.* **1965**, *140*, A1133.
- [59] H. Euchner, A. Groß, *Phys. Rev. Mater.* **2022**, *6*, 040302.
- [60] G. Kresse, J. Hafner, *Phys. Rev. B* **1993**, *47*, 558.
- [61] G. Kresse, J. Furthmüller, *Phys. Rev. B* **1996**, *54*, 11169.
- [62] G. Kresse, D. Joubert, *Phys. Rev. B* **1999**, *59*, 1758.
- [63] J. P. Perdew, K. Burke, M. Ernzerhof, *Phys. Rev. Lett.* **1996**, *77*, 3865.
- [64] P. E. Blöchl, *Phys. Rev. B* **1994**, *50*, 17953.
- [65] D. Sheppard, R. Terrell, G. Henkelman, *J. Chem. Phys.* **2008**, *128*, 134106.